Growth and characterization of Ba2LnFeNb4O15 (Ln = Pr, Nd, Sm, Eu) relaxor single crystals

Marjorie Albino, Philippe Veber, Stanislav Pechev, Christine Labrugère, Matias Velázquez, Mario Maglione, Michaël Josse

Growth and characterization of $Ba_2LnFeNb_4O_{15}$ (Ln = Pr, Nd, Sm, Eu) relaxor single crystals

Marjorie Albino[1,2], Philippe Veber[1,2], Stanislav Pechev[1,2], Christine Labrugère[1,2], Matias Velázquez[1,2], Mario Maglione[1,2], Michaël Josse[1,2]*

[1]CNRS, ICMCB, UPR 9048, F-33600 Pessac, France.

[2]Univ. Bordeaux, ICMCB, UPR 9048, F-33600 Pessac, France

Tetragonal Tungsten Bronze / Single crystal / Flux method / Relaxor / Modulated structure

ABSTRACT $Ba_2LnFeNb_4O_{15}$ (Ln = Pr, Nd, Sm and Eu) single crystals were grown from high temperature solution under controlled atmosphere. Chemical, structural and dielectric characterizations were performed on four crystals with tetragonal tungsten bronze (TTB) structure. The main difference between the four crystals compositions is the proportion of rare-earth, as well as vacancies, located in the square site. All crystals displayed an incommensurately modulated structure at room temperature in the paraelectric state. The corresponding basic structures were refined using the P4/mbm space group (R = 0.0274; 0.0416; 0.0328; 0.0357 for Ln = Pr, Nd, Sm and Eu respectively). Examination of the structural parameters confirmed the central role played by square-shaped channels in the crystal-chemistry of these materials. All crystals display a relaxor behaviour with T_m(1MHz) ranging from 110 to 270K. The chemical,

structural and physical properties of the crystals are discussed and compared, for the latter, with those of corresponding ceramics.

Introduction

Relaxor materials exhibit a large number of interesting dielectric properties, and the origin of the relaxor behaviour for the Tetragonal Tungsten Bronze (TTB) structure is debated in the literature[1]. Although the presence of different cations inside the same crystallographic sites has been found to trigger a relaxor effect in the SBN system[2-3] or in the $Ba_5LaTi_3Nb_7O_{30}$ compound[4], other driving forces have been proposed. The relaxor behaviour seems to depend on the radius ratio of the ions occupying the pentagonal and square channels in some systems[5], and of the size of the elements inserted in the octahedral sites in others[6]. The polarization of a large number of substituted relaxor compounds with TTB structure is caused by off-centering of the cations localized inside the octahedral sites. However it is obvious that other characteristics of the crystalline structure, particularly the cationic[7] and anionic[8] defects, the cationic distribution or cationic radii, impact the organization of dipolar moments. Moreover one can find reports in the literature, of octahedral distortions and rotations related to incommensurate modulated structures[9-11] which may also impact the dielectric properties.

In the case of the $Ba_2LnFeNb_4O_{15}$ (BLnFNO) TTB compounds, where Fe^{3+} and Nb^{5+} ions are distributed within the octahedral sites, the effect of the incorporation of rare-earth cations inside the square sites was highlighted by Josse *et al.*[12]. In fact, study of the BLnFNO ceramics showed that the accommodation of La^{3+} and Pr^{3+} in the TTB structure triggers a relaxor behaviour while the incorporation of smaller rare-earths, such as Nd^{3+}, Sm^{3+} and Eu^{3+}, induces a ferroelectric state. Further studies revealed original behaviours, such as ferroelectric to relaxor crossovers[13-16],

which led us to undertake the crystal growth of these BLnFNO TTBs, as single crystal studies should allow for a better comprehension of the dielectric behaviours encountered in this system.

Recently we have successfully developed a flux growth method[17], which was further optimized and allowed us to grow centimeter-sized $Ba_2LaFeNb_4O_{15}$ single crystals[18]. The present study report the use of this optimized growth process applied to the BLnFNO compositions where Ln = Pr, Nd, Sm and Eu. The crystal growth attempts of these materials are presented, and the chemical, structural and dielectric properties of the single crystals obtained are investigated and discussed, with respect to those of the corresponding ceramics concerning the dielectric properties.

1. Experimental methods

Quantitative analyses for Ba, Ln, Fe, and Nb contents on polished crystals were performed by electron probe micro-analysis EPMA (CAMECA SX100). The cationic contents were determined by assuming the full occupancy of the octahedral sites by Fe^{3+} and Nb^{5+} ions. Anionic content were calculated with respect to electroneutrality. For each composition, several single crystals underwent multiple tests to make sure the chemical compositions are homogeneous within a crystal and a batch. Chemical compositions were also determined from XRD data collected on BLnFNO single crystals.

X-ray photoelectron spectroscopy (XPS) measurements were carried out with a ESCALAB VG 220i-XL spectrometer using MgKα (hν = 1253.6 eV) radiation on as-grown crystals. Ar etching time of 0, 120, 360 and 720 sec. (etching speed ~0.2nm.s^{-1}) were used prior to data acquisition.

X-ray powder diffraction (XRPD) patterns at room temperature were used to identify the main and secondary phases stabilized following the crystal-growth process. Data collection was performed on a PANalitycal X'pert MPD Bragg-Brentano θ-2θ geometry diffractometer equipped

with a secondary monochromator over an angular range of 2θ = [8-80]°. The Cu-Kα radiation was used (λ = 1.5418 Å).

The crystallographic directions of the crystal surfaces were determined using X-ray Laue backscattering analysis (Mo source).

Single crystal XRD was performed with a Nonius Kappa CCD four circles diffractometer with monochromatized Mo-Kα radiation (λ = 0.71073 Å). Cell parameters, space group and modulation vectors were obtained from single crystals XRD data and the basic structure was refined in the P4/mbm space group with the WINGX program[19].

For dielectric measurements, crystals (1-2 mm in thickness) were polished and were annealed at 900°C for 3h[18], and silver electrodes were painted on (001) faces. Dielectric response from 80K to 400K was measured using a HP4194a impedance analyzer at frequencies ranging from 10kHz to 1MHz.

Throughout the manuscript, data from the study of BLaFNO crystals will be recalled as reference.

2. Crystal growth by the flux method

The BLnFNO solutes were first prepared by a conventional solid-state reaction method using starting materials barium carbonate $BaCO_3$ (Cerac, 99.9 %), lanthanide oxides Pr_6O_{11} and Ln_2O_3 with Ln = Nd, Sm and Eu (Cerac, 99.99%), iron oxide Fe_2O_3 (Rectapur, 99%), and niobium oxide Nb_2O_5 (LTS chemical, 99.95 %). Lanthanide oxides were dried overnight at 900°C to drive off hydroxyls groups prior to weighing. After mixing in stoichiometric proportions in an agate mortar and next by ball-milling in ethanol, the mixtures were calcined at 1280°C for 12h.

BLnFNO single crystals were grown with $LiBO_2$ flux under controlled atmosphere using the experimental conditions recently reported by Albino *et al.*[18]. The loads of 20g of 30mol.%

BLnFNO-70mol.% $LiBO_2$ powders were mixed and compressed uniaxially into pellets and placed into a platinum crucible which was then introduced in a sealed platinum chamber under a primary vacuum (P = 10^{-2} mbar). A thermal gradient about 0.5°C.cm^{-1} was achieved all along the platinum assembly placed into a resistive vertical furnace where the minimal temperature was set at the bottom of the inner crucible. The solutions were soaked at 1293°C during 24h. They were first cooled down to 1261°C at a rate of 0.4°C.h^{-1}, then heated quickly up to 1278°C, and finally cooled down to 1223°C at a rate of 0.2°C.h^{-1} in order to grow crystals with a significant size[18, 20].

Crystal growth attempts led to single crystals trapped into the remaining solidified loads. After removing $LiBO_2$ flux in hot HCl aqueous solution, BLnFNO brown/black single crystals were found at the top of the solidified solutions for each composition (Figure 1a) whereas the bottom of the charges did not melt (Figure 1b).

XRPD measurements performed on BLnFNO crushed crystals confirmed the TTB structure. Maghemite γ-Fe_2O_3 and fergusonites $LnNbO_4$ were observed (Figure 1c) and identified by XRPD as secondary phases for each growth. In addition, in the case of BEuFNO growth attempt, $Ba_3Fe_2Nb_6O_{21}$, with the Hexagonal Tungsten Bronze (HTB) structure (ICDD 79-0074), was also detected as sub-millimeter brown single crystals which may have grown within the non-molten part of the load.

As depicted in Figure 1b the estimated height of the non-molten part of the loads, located between the bottom of the inner crucible and the location of the first BLnFNO single crystals (h_{BPrFNO} = 2 mm; h_{BNdFNO} = 2.5 mm; h_{BSmFNO} = 4 mm and h_{BEuFNO} = 10 mm) increases with the molar mass of the solute. According to the low 0.5°C.cm^{-1} thermal gradient set in the furnace, we deduced that the 30 mol.% BLnFNO-70 mol.% $LiBO_2$ solidus temperatures for Ln = Pr, Nd, Sm, Eu are in the range 1293°C-1294°C and increase with the molar weight of the solute.

The decreasing height of the molten solution (from Pr to Eu) directly influence the BLnFNO growths, decreasing the yield of as-grown crystals, and also their typical size from (4.5 x 7 x 2) mm^3 for BPrFNO to (2 x 2 x 1) mm^3 for BEuFNO (Figure 2).

Laue back diffraction experiments were carried out on samples depicted in Figure 2 and revealed that they were actually single crystals. Laue patterns also revealed that the largest natural growth facet, whatever the considered rare earth ion, is perpendicular to the [001] direction.

3. Results and discussion

3.1. Chemical compositions

The compositions of BLnFNO crystals as determined by EPMA are listed in Table 1. Results show that chemical compositions of the crystals are different from the nominal composition (*i.e.* the composition of the load). In particular, the Ln content is significantly smaller than expected, especially in BSmFNO and BEuFNO crystals where it lies around 0.5 Ln per formula unit, *i.e.* even smaller than those of others crystals (0.9; 0.9 and 0.7 for La, Pr and Nd, resp.). For all the crystals, EPMA analyses show a relative stability of barium content, which probably remains inside the pentagonal sites, except for the Eu-based crystals. As for the octahedral sites, compositional analyses support a Nb excess, which can be understood as an adjustment of the Fe/Nb ratio. This adjustment is induced by the partial accommodation of Ln^{3+} ions, for sake of electroneutrality. It should be noted that the reduction of lanthanides and iron content is consistent with the formation of $LnNbO_4$ and γ-Fe_2O_3 secondary phases during the flux growth process.

3.2. X-ray photoelectron spectroscopy

We will present first the XPS study of $Ba_2La_{0.9}Fe_{0.8}Nb_{4.2}O_{15}$ (BLaFNO) crystals, never reported previously, as this compound is prototypical of the BLnFNO family.

The C*1s* peak (Figure 3a), visible on the BLaFNO crystal before Ar-ion etching, was used as the reference and was positioned at 284.7 eV[21]. The XPS method allowed for the observation of Ba^{2+} and Nb^{5+} ions at the surface of BLaFNO single crystal, while the detection of cations present in lower contents, *i.e.* La^{3+} and Fe^{3+}, was hindered by the C contamination (~ 64at.%). By comparison, the peaks observed after etching shift toward a lower binding energy after the first Ar-ion etching (120 sec.). This indicates that the local electronic environment of the corresponding atoms is affected by the etching.

As shown in Figure 3, the binding energies of Ba*3d* (781.0 eV), La*3d* (835.3 eV), Fe*2p* (707.4 eV), Nb*3d* (203.5 eV) and O*1s* (530.9 eV), as observed following a 120s etching, do not evolve with prolonged Ar-ion etching (above 120 sec.). XPS spectra on etched BLnFNO crystals are compatible with Ba^{2+} and Ln^{3+} ions, while if Nb^{5+} is the main oxidation state of niobium, other oxidation states (induced by etching as will be shown thereafter) are also observed, and finally the observations concerning Fe*2p* core-level suggest metallic iron. We will now comment in more detail each of these spectra.

For La$3d_{3/2}$ and La$3d_{5/2}$ core-level spectra, we observed on the Figure 3d double-peak structures, which were described as the charge-transfer effect from the ligand to the rare-earth *4f* orbitals due to the creation of the *3d* vacancy[22-23]. For each double peak present in the La*3d* spectra, the peak to a lower and a higher binding energy correspond to the bonding and antibonding orbital respectively.

As shown in Figure 3f, an additional Nb*3d* core level spectrum with lower binding energies appears and grows with the etching time. This is related to the reduction of Nb^{5+} ions by Ar ions, inducing the appearance of Nb^{4+} and Nb^{3+} ions. A similar phenomenon was previously observed

in potassium lithium niobate (KLN) crystal, although in this case the O*1s* line was also affected (it is not the case in the present study) and suggested that the creation of Nb^{4+} and Nb^{3+} ions is connected with the loss of oxygen[24]. Whether oxygen vacancies are involved or not, niobium reduction is certainly responsible for the surprising results concerning Fe*2p* core level spectrum, as the binding energies observed are consistent with metallic iron. Such a situation is rather unexpected in a dielectric, but appears consistent with observations in Fe/NbO thin films suggesting the propensity of iron to be reduced in the presence of niobium[25].

Line XPS spectra for all the constituting elements of BLnFNO single crystals (Ln = Pr, Nd, Sm, Eu), after 120 sec. Ar etching time, are reported in Figure 4. The shapes and positions of the observed signals are similar to what was observed for BLaFNO crystals, except for the Eu sample in which the O*1s* peak is significantly broader. To further investigate the chemical properties of BLnFNO crystals, peak fitting was performed using Gaussian-Lorentzian peak function with a gaussian component of [25-50]% and a lorentzian component of [25-50]%. For the Fe*2p* and Nb*3d* line spectra, three components related to the oxidation states of both elements were taken into account. Then the binding energy (BE) and the full width at half maximum (FWHM) for Ba, Ln, Fe and Nb were determined and reported in Table 2. Three components were also used for the analysis of O*1s* spectra, for which the results are gathered in Table 3.

The Ba*3d* and Ln*3d* (Ln = Pr, Nd, Sm) lines are consistent with the presence of Ba^{2+} and Ln^{3+} ions, respectively. The Eu*4d* line (not presented) is also consistent with the presence of Eu^{3+} in BEuFNO crystals. For all crystals, the higher energy peak associated to Nb^{5+} is positioned at ~208 eV, and signals associated to the smaller oxidation states (induced by Ar etching) are found at lower energies, close to ~203.5 eV for Nb^{3+} and ~205 eV for Nb^{4+}. The most prominent peaks are found for Nb^{5+} and Fe^{0}, while Nb^{4+}, Nb^{3+}, Fe^{2+} and Fe^{3+} display relatively small peaks. The equilibrium between iron and niobium oxidation states can be followed throughout the whole

series of crystals, as reported in Figure 5. The components associated to $Fe^{0,\ 2+,\ 3+}$ seem to be correlated to those associated to $Nb^{3+,\ 4+,\ 5+}$, as for example in BLaFNO a minimum concentration of Fe^{0} correspond to a maximum concentration of Nb^{5+}. As the reduction of Nb^{5+} cations to intermediate oxidation states by Ar etching was previously reported in the literature[24], one may consider that the reduction of iron is a secondary effect of niobium reduction, in which electrons are transferred from Nb^{3+} or Nb^{4+} ions to Fe^{3+} ions which are in turn reduced. Thus iron and niobium ions act as communicating vessels with respect to the reduction phenomenon. The smaller iron content found in BLnFNO, with Ln = Nd, Sm and Eu, could however induce a saturation of this equilibrium, or in other word, when iron vessel is (almost) fully reduced to a metallic state, the reduction of Nb^{5+} ions induced by Ar-etching is hindered. This reduction mechanism, as it is induced by Ar ions etching, is of little interest with respect to dielectric materials. However TTBs are also studied as mixed conductors[26], and may present opportunities for the development of thermoelectrics[27]. Our observations suggest that the association of iron and niobium could be a way to enhance such kind of properties in TTBs.

The O*1s* core level spectrum visible in Figure 4 can be deconvoluted in three components, which correspond to (Fe,Nb)-O, Ln-O and Ba-O bonds, from higher to lower binding energy respectively (Table 3). The relative areas of these three components evolves within the BLnFNO series, the (Fe,Nb)-O component increasing from La to Eu, while the Ba-O component decreases, but the evolution of the Ln-O is difficult to analyze, except for the Eu-O component which is responsible for the broadening of the O*1s* line in BEuFNO. The (Fe,Nb)-O component (and thus the corresponding environment) appears very stable in shape and position throughout the BLnFNO series, while the Ba-O component, stable in position, is broadened when going from La to Nd, and stable afterwards. The width of the Ln-O component can hardly be rationalized, but its position appears to shift towards higher binding energies for Ln = Sm and Eu.

Overall, the XPS study show that the oxidation states of Ba and Ln elements are consistent with the ones expected, and that niobium and iron are successively reduced due to Ar ions etching. The environment of oxide anions is essentially stable throughout the series for (Fe,Nb)-O and Ba-O bonds, although a complicated evolution is observed for Ln-O bonds.

3.3. XRD on single crystals

XRD on BLnFNO single crystals at room temperature revealed that they retain the TTB structure (Table 4), despite the variation of their chemical composition, and adopt an incommensurately modulated structure, the basic structure of which can be described in the space group P4/mbm (n°127). The modulation is bidimensionnal and is characterized by modulation vectors $q_1 = \alpha, \alpha, ½$ and $q_2 = \alpha, -\alpha, ½$. The modulation parameter, α, was found almost identical, at room temperature, for all the TTB crystals of the BLnFNO series. It should be noted that α values, 0.290(5) for Ln = La, Pr, Nd and 0.280(5) for Sm and Eu were extracted from the initial automatic search procedure, but were not further refined.

Refinement of XRD data was carried out only for the basic TTB structure in the space group P4/mbm. Initially, cationic positions were assumed to be fully occupied with no cross-substitution. In order to obtain a consistent estimate of the occupancies, the two octahedral sites (M(1) and M(2)) were both assumed to be i)fully occupied and ii)statically occupied by iron and niobium ions. Tentative refinements confirmed that the pentagonal sites were fully occupied by barium. The Ba position was split (x and y coordinates being no longer correlated), as frequently encountered[28]. The possibility of cross-substitution between Ba and Ln sites, the latter occupying the square sites, was ruled out by tentative refinements, even in BEuFNO crystals, in which EPMA results suggested the presence of barium in the square sites. The iron/niobium ratio and the lanthanide contents were then refined with restraints set for sake of electroneutrality. Anionic

positions were assumed to be fully occupied throughout the whole refinement process. Cell parameters, unit cell volume, and agreement factors for BLnFNO crystals are given in Table 4.

One could expect a decrease of the *a* and *c* lattice parameters from La- to Eu-based compounds with respect to the reduction of Ln^{3+} ionic radius, and this trend is observed for Ln = La, Pr and Nd. Nevertheless, smaller Eu^{3+} and Sm^{3+} cations are associated with significantly larger cells than their Nd^{3+} counterparts, although high Ln^{3+} vacancies contents could imply unit cell expansion for $Ba_2Sm_{0.60(1)}\square_{0.40(1)}Fe_{0.41(1)}Nb_{4.59(1)}O_{15}$ and $Ba_2Eu_{0.60(1)}\square_{0.40(1)}Fe_{0.39(1)}Nb_{4.61(1)}O_{15}$ crystals. It is remarkable that the chemical compositions of the crystals within the BLnFNO series (Ln = La, Pr, Nd, Sm, Eu, Table 5) can be described by the formulation $Ba_2Ln_{1-x}\square_xFe_{1-3x/2}Nb_{4+3x/2}O_{15}$, which is somewhat reminiscent of the formulation $Ba_{2-x/8}Ln_{1-x}\square_xFe_{1-3x/2}Nb_{4+3x/2}O_{15-x/8}$ found in corresponding ceramics.

The niobium and lanthanides occupancies refined from XRD data are consistent with those extracted from EPMA analysis (Figure 6), and thus the hypotheses of a fully occupied octahedral framework (EPMA and XRD) and the restraints applied on Fe/Nb ratio and Ln contents in XRD refinements are validated. The EPMA and XRD results clearly show that the square tunnels are partially occupied by Ln^{3+} ions, and that the niobium content in the octahedral sites increases from BLaFNO to BEuFNO. These observations are in agreement with the formation of secondary phases ($LnNbO_4$ and γ-Fe_2O_3) during the growth, as reported in part 2. Thus the variation of the lanthanide content in the square sites is associated with a higher content of ferroelectrically active Nb^{5+} cations, especially in BSmFNO and BEuFNO crystals. It is worth mentioning that iron and niobium atoms are localized inside regular M(1) and distorted M(2) octahedral sites, the latter being prone to bear a dipole moment.

In BLnFNO single crystals the barium atoms are in the pentagonal sites, the lanthanides in the square sites, the triangular site is empty and both M(1) and M(2) octahedral sites are occupied by

a statistical distribution of iron and niobium, as reported in Table 6. A representation of the overall structure, showing polyhedral linking and the anisotropic displacement parameters (represented by ellipsoids), is given for BPrFNO in Figure 7. The ellipsoids associated to the anionic framework are the largest ones, suggesting that the modulation strongly affects the anionic sublattice. One can also clearly see, from Figure 7, the distortion of the M(2) site related to the accommodation of the Ln^{3+} ions within the square channels. Thus the XRD study shows that in BLnFNO crystals, the structural distortion is undoubtedly influenced by both parameters, Ln^{3+} cation radius, as illustrated by Figure 7, and vacancies content, as illustrated by the evolution of cell volume (Table 4), both being located in the square channels, the central role of which concerning TTBs crystal chemistry was previously pointed out[12]. Further crystal chemical considerations, from detailed analysis of atomic and bonding parameters, confirm these trends. In Figure 8 can be found the identification of the various parameters discussed below.

3.3.1. Atomic parameters

The atoms are distributed in layers located at z=0 (Nb, Fe, O(2), O(3), O(4)) and z=1/2 (Ln, Ba, O(1) et O(5)), which allows for comparison of their positions within the series of BLnFNO single crystals. The modifications of positional parameters are rather small, and systematically below 0.5%. The relative variations of O(3) and M(2) positional parameters (with respect to the corresponding BLaFNO parameters), which display the largest variations within the series, are displayed in Figure 9a.

While the evolution of M(2) positional parameters appears quite monotonous, those of O(3) are strongly modified in BSmFNO and BEuFNO single-crystals. This singular evolution, with respect to La, Pr and Nd representatives, may be related to the high vacancies content (40%) in these samples.

For atoms located at z=0, the amplitude of their shifts, is related to their distance from the square channel accommodating the rare earth ions, as schematized in Figure 9b. This trend is confirmed for atoms located at z=1/2 (not represented), for which O(5) in distorted M(2) octahedral sites displays the largest shifts.

The trend observed for atomic position is also relevant concerning the atomic displacement parameters of the anionic framework. At z=1/2, U_{11}O(5), for the oxygen closest to the square channels, ranges from 0.079(5) (La) to 0.158(16)Å² (Nd) in the BLnFNO series, while for all the others oxygen atoms, U_{11} is systematically smaller than 0.07Å². At z=0, U_{33}O(3), for the oxygen which delimits the square channels, vary from 0.059(4) (La) to 0.129(10)Å² (Eu) in the BLnFNO series, while U_{33} is systematically smaller than 0.07Å² for all the others oxygen atoms. As illustrated by the ellipsoids in Figure 7, the large atomic displacement parameters of O(3) and O(5) may be related to a tilting of the [M(2)O_6] octahedra which define the square channel of the TTB structure.

3.3.2. Bond length

Overall, the Ba-O and M-O bond length appear rather stable within the series, with Ba-O distances variations being smaller than 0.026Å (with the exception of Ba-O(3) distances with a 0.056Å variation), and M-O distances variations being smaller than 0,017Å (with the exception of M(2)-O(3) (0.049Å) and M(2)-O(3)' (0,042Å)). However both Ln-O(3) and Ln-O(5) distances vary by slightly more than 0.05Å within the series.

It is remarkable that bond length involving either the Ln^{3+} ions (located in the square channels at z=1/2) or the O(3) independent oxygen atoms (defining the square channel at z=0) display the largest variations, emphasizing again the central role of this channel in the crystal chemistry of BLnFNO TTBs.

The influence of Ln vacancies can be seen in the increase of Ln-O bond lengths observed for BSmFNO and BEuFNO (Figure 10).

A further look at the evolution of cation-anion distances also shows that Ln-O and Ba-O distances evolve in opposite ways. This observation brings support to the idea that the ionic radii ratio of B (square) to A (pentagonal) sites is a relevant crystal-chemical parameter for the TTB structure[1, 16].

There is also some subtle differences in the evolution of M(2)-O(3) and M(2)-O(3)' bond lengths, the former being rather monotonous with respect to Ln^{3+} ionic radii, while the latter behaves differently for Sm and Eu-based crystals. This observation supports the results of previous studies emphasizing the role of vacancies, inside both square and pentagonal sites, in the crystal chemistry of TTBs[29].

3.3.3. Bonding angles

The largest variations among intra- and inter-polyhedra bonding angles in the BLnFNO series are found within the $[M(2)O_6]$ octahedra, with a 6% opening of the O(3)-M(2)-O(3)' angle (from 81.2(3)° (La) to 86.1(5)° (Sm)) and a 2.8% closing of the opposite O(4)-M(2)-O(2) angle (from 97.8(2)° (La) to 95.1(3)° (Eu)). As $[M(2)O_6]$ octahedra define the square channels in the TTB framework, these observation again evidence its central role in BLnFNO TTBs crystal chemistry. Further details of the evolution of the angles associated to the $[M(2)O_6]$ octahedra are displayed in Figure 11.

Within the octahedron, the variation of O(3)-M(2)-O(3)' and O(4)-M(2)-O(2) angles can be linked to the distortions of the $[M(2)O_6]$ octahedron itself, in relation with the species accommodated in the square channels. It is remarkable that while the former evolves

discontinuously, and is likely to be affected by vacancies content, the latter display a rather continuous evolution, which appears closely related to Ln^{3+} ionic radius.

Furthermore the variation of the M(2)-O(3)-M(2) angle can be related to correlated rotations of these octahedra associated with the accommodation of the species located in the square channels. The widest opening of this angle is found in Sm and Eu crystals, which accommodate a large amount of vacancies. This again supports the idea that vacancies within the square channels have to be accounted for, when investigating the crystal chemistry of TTBs.

3.4. Dielectric properties

The temperature dependence of the real and imaginary parts of the dielectric permittivity of BLnFNO (Ln = Pr, Nd, Sm and Eu) crystals, in the frequency range 10kHz-1MHz, is displayed in Figure 12. All the crystals display notably larger maximum permittivities (from 400 to 1700, at 10kHz) than those observed in ceramics (from 180 to 700, at 10kHz[12]). Significant dielectric losses can clearly be seen at room temperature in the imaginary part of the dielectric permittivity $\varepsilon'' = f(T)$, which may be related, for example, to electron hopping within the octahedral framework, as it is statistically occupied by Fe^{3+} and Nb^{5+} ions.

Before the onset of these dielectric losses, a dielectric transition takes place, with a very specific signature, common to all crystals. As frequency increases, the temperature of the maximum of permittivity, T_m is shifted to higher temperature while the permittivity decreases. This causes the transition to be spread over a wide range of temperatures, while far below and far above the transition, the permittivity remains rather frequency independent. These phenomena reveal that these TTB crystals have a typical relaxor behaviour, as the rather low dielectric losses below these transitions ($\tan\delta < 10\%$) do not support extrinsic mechanisms such as Maxwell-Wagner relaxation. The temperature corresponding to the maximum value of the dielectric

constant at a given frequency is shifted to lower temperatures with the increase in Ln^{3+} ionic radius.

The T_m at 1MHz for BLnFNO crystals with Ln = La, Pr, Nd, Sm and Eu are displayed in Figure 13, along with the evolution of the normalized dielectric permittivity. One can clearly see the similarity of the dielectric response throughout the BLnFNO series, and the quite monotonous evolution of T_m(1MHz) which decreases from Eu to La. The maximum value of the permittivity at 10kHz (Figure 14a) also decreases with increasing Ln^{3+} ionic radius, from Eu^{3+} (1.066 Å) to La^{3+} (1.16 Å). Here the Ln^{3+} ionic radius obviously has the most influence, as the maximum permittivity is obtained for BEuFNO (~1700), although in this crystal the square channel encompasses as much as 40% of vacancies. As can be seen from Figure 14b, the dielectric dispersion associated to the relaxor behaviour of BLnFNO crystals, which can be described by $\Delta T_m = T_m(500Hz) - T_m(1MHz)$, decreases with the increase of lanthanides ionic radius. The specific feature detected for the BPrFNO crystals, with almost no dispersion apparent in the real part of the permittivity, is related to the contribution of dielectric losses. Although the dispersion is actually small for the BPrFNO crystal, an obvious dielectric dispersion can be seen in the imaginary part of the permittivity. One can also note that the evolution of T_m(1MHz) is almost linear with respect to Ln^{3+} ionic radius, contrary to the evolution of the dielectric permittivity.

These results show that the dielectric permittivity of BLnFNO TTBs is strongly dependent on the Ln^{3+} radius, as is T_m(1MHz). The amplitude of the dielectric dispersion associated to the relaxor behaviour may be controlled either by Ln^{3+} ionic radius, by the vacancies content or by both parameters, as it reaches maxima for the smallest rare earths studied and for the largest vacancies content. Once again, however, the square channels, and the Ln^{3+} ions and vacancies accommodated within, obviously play a central role concerning the dielectric properties.

3.5. Discussion

The BLnFNO crystals (Ln = Pr, Nd, Sm, Eu) obtained by flux method present significant deviations from the target compositions, stronger than those observed in the corresponding ceramics. However their chemical compositions can be rationalized, in a similar way to the one used for ceramics, by the formulation $Ba_2Ln_{1-x}\square_xFe_{1-3x/2}Nb_{4+3x/2}O_{15}$ (from x=0.16 for Ln = Pr to x=0.40 for Ln = Eu). In these crystals, the barium and lanthanides oxidation states are consistent with the expectations, while the XPS study highlighted the propensity of iron to be reduced in the presence of niobium. This observation could be related to the important dielectric losses observed in all the BLnFNO crystals at room temperature. Actually they are prepared in a reducing atmosphere and usually bear some oxygen vacancies, that can cause the niobium and iron ions to be reduced. However the oxygen vacancies can be cured, to some extent, by subsequent annealing in oxygen.

The BLnFNO single crystals retain the TTB structure, and display a bidimensionnal incommensurate modulation which was not solved nor refined in the present study. It is remarkable that these modulations share (almost) the same modulation parameter $\alpha \approx 0.29$. This value is nonetheless consistent with those reported in the literature ($0.25<\alpha<0.31$)[9-11, 30-34]. The main feature of the incommensurate modulations in TTBs is cooperative tiltings in the octahedral framework[9-11, 28], which are likely to affect any kind of polar order the TTB framework may possess.

The basic structure of BLnFNO crystals was refined, and the strongest structural variations were found around the square channels in which Ln^{3+} ions and vacancies are accommodated. A survey of several crystal chemical parameters (atomic positions, bond length...) has confirmed the central role of the square channels in the crystal chemistry of BLnFNO TTBs. The atomic

positions and displacement parameters, in particular, display variations which scale with the proximity of the considered atom with the square channel. The crystal chemistry of TTBs, however, can not be reduced to this square channel, and must account for the contributions of other features of the TTB framework (pentagonal channels, cationic framework...), in order to build a complete understanding of the TTB matrix. In this view, some crystal chemical parameters pointed out in the literature (ionic radii ratio of cations occupying the square and pentagonal channels[1, 16], vacancies content[29]...) are supported by some of our observations. In the end, it is likely that the accommodation of the species inserted in the square channel, depending on their content and the characteristics of the species occupying the other channels of the TTB structure, plays an important role in the onset of aperiodic modulations.

All the BLnFNO crystals display a relaxor behaviour, in contrast with the ferroelectric response previously observed in $Ba_2LnFeNb_4O_{15}$ ceramics with Ln = Nd, Sm and Eu[12]. Larger dielectric permittivities (up to ε'=1700) than those of corresponding ceramics are also found in all the crystals. It is unclear, however, if these higher permittivities arise from chemical (compositional variation), crystalline (larger dielectric permittivities in single-crystals due to measurement along a specific [001] direction) or microstructural (limitation of ceramics permittivities by microstructure and secondary phases) phenomena. At this stage of the study, it is difficult to establish connections between the relaxor behaviour and modulated TTB structure, as the latter is still present at room temperature in the paraelectric state. However modulated structures usually evolve with temperature, and thus may indirectly affect the dielectric state of BLnFNO crystals.

Meanwhile the TTB crystal structure and dielectric properties remain highly sensitive to the content of the square channels, in agreement with previous studies[10]. The dielectric transition temperatures of TTB crystals increase linearly with the decrease of Ln^{3+} ionic radius, but also

with the increase of Nb^{5+} content, as illustrated by the afore-mentioned formulation. However the much higher contents of ferroelectrically active ions inside the octahedral sites is not necessarily the driving force of the relaxor behaviour, as in some ceramics its increase is associated with the disappearance of a ferroelectric state[14]. It is thus extremely interesting to compare the dielectric transitions temperatures and the content of the square sites, as observed in BLnFNO crystals and in the corresponding ceramics, with respect to Ln^{3+} ionic radius (Figure 15).

The main difference between crystals and ceramics chemical compositions is the Ln^{3+} content within the square sites, which reach values as low as 60% in BSmFNO and BEuFNO crystals, *vs* 81% in BEuFNO ceramics[35]. As the single crystals were grown from a liquid phase containing a flux, and thus compositional modifications were easier, one can consider that the composition of the BLnFNO crystals are the most stable ones. Meanwhile, for Nd, Sm and Eu ceramics, in which the Ln^{3+} content is higher, the compositional modifications were somehow limited by the mechanism compensating the Ln^{3+} deficit and producing the secondary phases. The compensation mechanism for the ceramics can be resumed as follows:

$$\mathbf{Ba_{2-x/8}Ln_{1-x}\square_{x}Fe_{1-3x/2}Nb_{4+3x/2}O_{15-x/8} + x\ LnNbO_4 + 3x/24\ BaFe_{12}O_{19}}$$ [36]

while the compensation mechanism for the single crystals would be:

$$\mathbf{Ba_2Ln_{1-x}\square_{x}Fe_{1-3x/2}Nb_{4+3x/2}O_{15} + x\ LnNbO_4 + 3x/4\ \gamma\text{-}Fe_2O_3}$$

In fact, the difference between Ln^{3+} deficit compensation mechanisms in ceramics and single crystals lies in the involvement of Ba^{2+} ions, as the $BaFe_{12}O_{19}$ phase is formed in ceramics (responsible of their composite multiferroic properties[37]), while γ-Fe_2O_3 is formed during the growth of single crystals.

While the Ln^{3+} ionic radius appears to control the ordering temperature in crystals, as a rather linear evolution of both parameters is found (Figure 15), the vacancies content obviously affects the range of the polar order. This latter point is illustrated by the relaxor behaviour found in

BNdFNO crystals (Nd content: 76%), while BNdFNO ceramics are ferroelectric (Nd content: 100%). There is however limits to the impact of vacancies on the dielectric behaviour, as BLaFNO and BPrFNO crystals and ceramics (84% ≤ Ln content ≤ 100%) are relaxors. Furthermore, although BSmFNO and BEuFNO encompass similar Ln^{3+} contents, and display larger cell volumes than their Nd analogue, the ordering temperature increase from BSmFNO to BEuFNO, supporting the prevalence of Ln^{3+} ionic radius on the dielectric behaviour of BLnFNO TTBs. Thus, the BLnFNO single crystals offer a solid basis to investigate the underlying mechanism of relaxor behaviour in $Ba_2LnFeNb_4O_{15}$ TTBs, but may also give hints on the most important parameters controlling the composition of TTB materials, the expression of ferroelectric properties and ultimately the formation of multiferroic "crystal chemical composites".

4. Conclusion

We successfully grew millimeter- to centimeter-sized BLnFNO single crystals with the TTB structure by using a high temperature solution growth method performed under controlled atmosphere. The growth conditions allowed locating the solidus (1293 to 1294°C) for the 30 mol.% BLnFNO- 70 mol.% $LiBO_2$ region of the phase diagrams. Two secondary phases, namely fergusonite $LnNbO_4$ and maghemite γ–Fe_2O_3 were invariably detected whatever the rare earth element Ln = Pr, Nd, Sm, Eu involved.

The chemical compositions of the crystals strongly deviate from the nominal composition, due to partial accommodation of Ln^{3+} ions within the square sites of the TTB framework. This induces high concentrations of vacancies in the square channels, reaching 40% for Ln = Sm, Eu. The deviation from the nominal composition can be described by the following formulation: $Ba_2Ln_{1-x}\square_xFe_{1-3x/2}Nb_{4+3x/2}O_{15}$. This formulation is consistent with the composition of all

BLnFNO crystals (Ln = La, Pr, Nd, Sm and Eu), as determined by EPMA and XRD, and accounts for the secondary phases formation.

XPS studies indicated that Ba and Ln oxidation states are consistent with the expected values, while reduction of iron and niobium due to Ar etching suggest hopping as the mechanism responsible for the dielectric losses observed at room temperature in all crystals. Structural investigations performed by single-crystal XRD revealed an incommensurately modulated structure at room temperature in all crystals. The basic structure was refined in the P4/mbm space group, and the results obtained allowed for the examination of several crystal chemical parameters. While some of our observations supports the relevance of some parameters concerning the crystal chemistry of TTBs, the central role played by the square channel in BLnFNO TTBs has been confirmed.

The dielectric measurements performed on crystals equipped with electrodes perpendicular to the [001] direction revealed a relaxor behaviour in all BLnFNO crystals (Ln = Pr, Nd, Sm and Eu), which are thus good candidates for the study of the driving forces concerning relaxor behaviour in TTBs. Finally comparison of the dielectric transition temperatures and lanthanide contents of the BLnFNO crystals and of the corresponding ceramics confirm the prevalent role of the square channels (and the species accommodated wherein) on the dielectric properties of BLnFNO TTBs. Our observations also suggest that these crystals may provide further understanding of TTBs, especially concerning the parameter controlling their chemical composition, their ferroelectric and ultimately multiferroic composite properties.

5. Acknowledgements

The authors acknowledge financial supports from the Centre National de la Recherche Scientifique (CNRS), Aquitaine region (Grant 20091101010) and the Agence National de la Recherche (ANR CROCODIEL) (Grant ANR-09-JCJC-0079). Crystal Growth platform acknowledges the financial support of GIS AMA "Advanced Materials in Aquitaine". The authors wish to thank Viraphong Oudomsack for Pt assembly soldering. Michel Lahaye is acknowledged for the EPMA characterization of the crystals.

REFERENCES

(1) Shvartsman, V. V.; Lupascu, D. C. Lead-free relaxor ferroelectrics. *J. Am. Ceram. Soc.* **2012**, *95 (1)*, 1-26.

(2) Glass, A. M. Investigation of the electrical properties of $Sr_{1-x}Ba_xNb_2O_6$ with special reference to pyroelectric detection. *J. Appl. Phys.* **1969**, *40*, 4699-4713.

(3) Kakimoto, K.; Kakemoto, H.; Baba, A.; Fujita, S.; Masuda, Y. Synthesis and dielectric properties of $Sr_xBa_{1-x}Nb_2O_6$ formed by YAG laser ablation. *J. Eur. Ceram. Soc.* **2001**, *21*, 1569-1572.

(4) Li, K.; Zhu, X. L.; Liu, X. Q.; Chen, X. M. Relaxor ferroelectric characteristics of $Ba_5LaTi_3Nb_7O_{30}$ tungsten bronze ceramics. *Appl. Phys. Lett.* **2012**, *100*, 012902.

(5) Zhu, X. L.; Chen, X. M.; Liu, X. Q.; Li, X. G. Dielectric relaxations, ultrasonic attenuation, and their structure dependence in $Sr_4(La_xNd_{1-x})_2Ti_4Nb_6O_{30}$ tungsten bronze ceramics. *J. Mater. Res.* **2008**, *23*, 3112-3121.

(6) Rotaru, A.; Arnold, D. C.; Daoud-Aladine, A.; Morrison, F. D. Origin and stability of the dipolar response in a family of tetragonal tungsten bronze relaxors. *Phys. Rev. B* **2011**, *83*, 184302.

(7) Yao, Y. B.; Mak, C. L.; Ploss, B. Phase transitions and electrical characterizations of $(K_{0.5}Na_{0.5})_{2x}(Sr_{0.6}Ba_{0.4})_{5-x}Nb_{10}O_{30}$ (KNSBN) ceramics with 'unfilled' and 'filled' tetragonal tungsten-bronze (TTB) crystal structure. *J. Eur. Ceram. Soc.* **2012**, *32*, 4353-4361.

(8) Prades, M.; Masó, N.; Beltrán, H.; Cordoncillo, E; West, A R. Synthesis, structural characterization, and electrical properties of new oxygen-deficient tetragonal tungsten bronzes $Ba_2NdTi_{2+x}Nb_{3-x}O_{15-x/2}$. *Inorg. Chem.* **2013**, *52*, 1729-1736.

(9) Woike, Th.; Petricek, V.; Dusek, M.; Hansen, N. K.; Fertey, P.; Lecomte, C.; Arakcheeva, A.; Chapuis, G.; Imlau, M.; Pankrath, R. The modulated structure of $Ba_{0.39}Sr_{0.61}Nb_2O_6$. I. Harmonic solution. *Acta Crystallogr.* **2003**, *B59*, 28-35.

(10) Surmin, A.; Fertey, P.; Schaniel, D.; Woike, T. Modulated structure of potassium sodium strontium barium niobates (KNSBN) : harmonic solution. *Acta Crystallogr.* **2006**, *B62*, 228-235.

(11) Graetsch, H. A.; Pandey, C. S.; Schreuer, J.; Burianek, M.; Mühlberg, M. Incommensurate modulation of calcium barium niobate (CBN28 and Ce:CBN28). *Acta Crystallogr.* **2012**, *B68*, 101-106.

(12) Josse, M.; Bidault, O.; Roulland, F.; Castel, E.; Simon, A.; Michau, D.; Von der Mühll, R.; Nguyen, O.; Maglione, M. The $Ba_2LnFeNb_4O_{15}$ "tetragonal tungsten bronze": Towards RT composites multiferroics. *Solid State Sci.* **2009**, *11*, 1118-1123.

(13) Castel, E.; Josse, M.; Michau, D.; Maglione, M. Flexible relaxor materials: $Ba_2Pr_xNd_{1-x}FeNb_4O_{15}$ tetragonal tungsten bronze solid solution. *J. Phys.: Condens. Matter* **2009**, *21*, 452201.

(14) Roulland, F.; Josse, M.; Castel, E.; Maglione, M. Influence of ceramic process and Eu content on the composite mutiferroic properties of the $Ba_{6-2x}Ln_{2x}Fe_{1-x}Nb_{9-x}O_{30}$ TTB system. *Solid State Sci.* **2009**, *11*, 1709-1716.

(15) Kinka, M.; Josse, M.; Castel, E.; Bagdzevicius, S.; Samulionis, V.; Grigalaitis, R.; Banys, J.; Maglione, M. Coexistence of ferroelectric and relaxor states in $Ba_2Pr_xNd_{1-x}FeNb_4O_{15}$ ceramics. *IEEE Trans. Ultrason., Ferroelec. Freq. Contr.* **2012**, *59(9)*, 1879-1882.

(16) Albino, M. Synthèse et caractérisation structurale et diélectrique de céramiques et de monocristaux relaxeurs de structure TTB. Ph.D. Thesis, Bordeaux University, September 2013.

(17) Castel, E.; Veber, P.; Albino, M.; Velázquez, M.; Pechev, S.; Denux, D.; Chaminade, J. P.; Maglione, M.; Josse, M. Crystal growth and characterization of tetragonal tungsten bronze ferroniobates $Ba_2LnFeNb_4O_{15}$. *J. Cryst. Growth* **2012**, *340*, 156-165.

(18) Albino, M.; Veber, P.; Castel, E.; Velázquez, M.; Schenk, K.; Chapuis, G.; Lahaye, M.; Pechev, S.; Maglione, M.; Josse, M. Growth and characterization of centimeter-sized $Ba_2LaFeNb_4O_{15}$ crystals from high-temperature solution under a controlled atmosphere. *Eur. J. Inorg. Chem.* **2013**, *15*, 2817-2825.

(19) Farrugia, L. J. WinGX suite for small-molecule single-crystal crystallography. *J. Appl. Cryst.* **1999**, *32*, 837-838.

(20) Elwell, D.; Scheel, H. J. Crystal Growth from High-Temperature Solutions, Academic Press, London, 1975.

(21) Wagner, C. D.; Riggs, W. M.; Davis, L. E.; Moulder, J. F.; Muilenberg, G. E. Handbook of X-ray Photoelectron Spectroscopy, Perkin-Elmer, Minneapolis, MN, 1979.

(22) Suzuki, C.; Mukoyama, T., Kawai, J.; Adachi, H. Calculation for the charge-transfer effect of La compounds in the $3d^{-1}$ core-hole state. *Phys. Rev. B* **1998**, *57*, 9507-9514.

(23) Suzuki, C., Kawai, J., Takahashi, M.; Vlaicu, A. M.; Adachi, H.; Mukoyama, T. The electronic structure of rare-earth oxides in the creation of the core hole. *Chem. Phys.* **2000**, *253*, 27-40.

(24) Jun, B. E.; Kim, C. S.; Kim, H. K.; Kim, J. N.; Hwang, Y. H. Ar-ion etching effects on the XPS spectra of the ferroelectric potassium lithium niobate crystal. *J. Korean Phys. Soc.* **2005**, *46*, 100-103.

(25) Wong, P. C.; Wong, K. C.; Li, Y. S.; Mitchell, K. A. R. XPS observations of the accelerated oxidation of niobium in the presence of iron. *Surf. Rev. Lett.* **1995**, *02*, 495-500.

(26) Kaiser, A.; Bradley, J. L.; Slater, P. R.; Irvine, J. T. S. Tetragonal tungsten bronze type phases $(Sr_{1-x}Ba_x)_{0.6}Ti_{0.2}Nb_{0.8}O_{3-\delta}$: Material characterisation and performance as SOFC anodes. *Solid State Ionics* **2000**, *135*, 519-524.

(27) Lee, S. ; Bock, J. A. ; Trolier-McKinstry, S.; Randall, C. A. Ferroelectric-thermoelectricity and Mott transition of ferroelectric oxides with high electronic conductivity. *J. Eur. Ceram. Soc.* **2012**, *23*, 3971-3988.

(28) Jamieson, P. B.; Abrahams, S. C.; Bernstein, J. L. Ferroelectric tungsten bronze-type crystal structures. II. Barium sodium niobate $Ba_{(4+x)}Na_{(2-2x)}Nb_{10}O_{30}$. *J. Chem. Phys.* **1969**, *50*, 4352-4363.

(29) Belous, A.; V'yunov, O.; Mishchuk, D.; Kamba, S.; Nuzhnyy, D. Effect of vacancies on the structural and relaxor properties of (Sr,Ba,Na)Nb_2O_6. *J. Appl. Phys.* **2007**, *102*, 014111.

(30) Schneck, J.; Denoyer, F. Incommensurate phases in barium sodium niobate. *Phys. Rev. B* **1981**, *23*, 383-388.

(31) Graetsch, H. A.; Schreuer, J.; Burianek, M.; Mühlberg, M. Thermally induced structural changes in incommensurate calcium barium niobate $Ca_{0.28}Ba_{0.72}Nb_2O_6$ (CBN28). *J. Solid State Chem*. **2012**, *196*, 255-266.

(32) Labbé, Ph.; Leligny, H.; Raveau, B; Schneck, J.; Tolédano, J. C. X-ray structural determination of the quasi-commensurate phase of barium sodium niobate. *J. Phys.: Condens. Matter*, **1989**, *2*, 25-43.

(33) Bursill, L. A.; Lin, P. J.; *Acta Crystalogr.* Incommensurate superstructures and phase transition of strontium barium niobate (SBN). **1987**, *C43*, 49-56.

(34) Peng, J. L.; Bursill, L. A.; *Acta Crystallogr.* Superlattice structure of ferroelectric barium sodium niobate (BNN). **1987**, *B43*, 504-512.

(35) Castel, E. Synthèse de nouveaux matériaux multiferroïques au sein de la famille des bronzes quadratiques de formule $Ba_2LnFeNb_4O_{15}$. Ph.D. Thesis, Bordeaux University, November 2009.

(36) Josse, M. Des fluorures aux ferroïques : l'empire de la cristallochimie, Habilitation à Diriger les Recherches, Bordeaux University, December 2012.

(37) Castel, E.; Josse, M.; Roulland, F.; Michau, D.; Raison, L.; Maglione, M. In-situ formation of barium ferrite in iron-doped "tetragonal tungsten bronze" : Elaboration of room temperature multiferroic composites. *J. magn. magn. mater.* **2009**, *321*, 1773-1777.

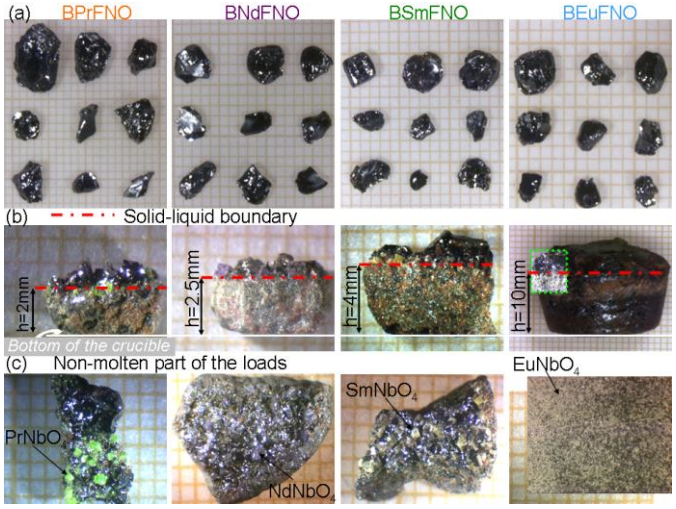

Figure 1. (a) As-grown BLnFNO crystals, shown on millimetric paper.

(b) Longitudinal cuts of the bottom part of the remaining solidified loads, after the growth attempts of BLnFNO with Ln = Pr, Nd, Sm, and Eu. For this latter one, the part surrounded by a green rectangle shows more cleary the solid-liquid boundary. The distance h corresponds to the non-molten height of the loads, taken between the bottom of the inner crucible and the location of the first BLnFNO single crystals visually detected.

(c) Fergusonite $LnNbO_4$, where Ln = Pr, Nd, Sm and Eu, and corresponding respectively to green, purple, yellowish and white crystals.

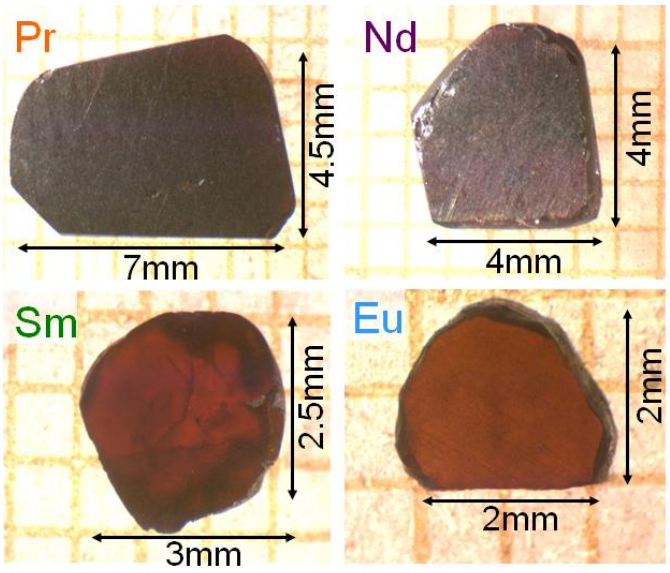

Figure 2. Post-annealed BLnFNO (Ln = Pr, Nd, Sm and Eu) crystals used for the dielectric measurements.

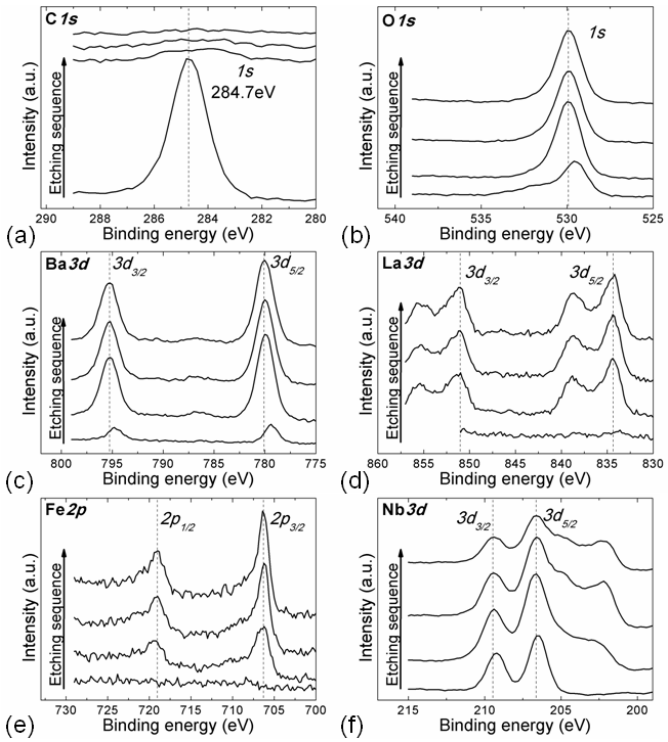

Figure 3. XPS spectra evolution following Ar-ion etching on a BLaFNO crystal. The etching sequence from bottom to top shows each core level after Ar-ion-etching times at 0, 120, 360 and 720 sec. Figures show the line spectra of (a) C*1s*, (b) O*1s*, (c) Ba$3d_{3/2}$ and Ba$3d_{5/2}$, (d) La$3d_{3/2}$ and La$3d_{5/2}$, (e) Fe$2p_{1/2}$ and Fe$2p_{3/2}$, (f) Nb$3d_{3/2}$ and Nb$3d_{5/2}$.

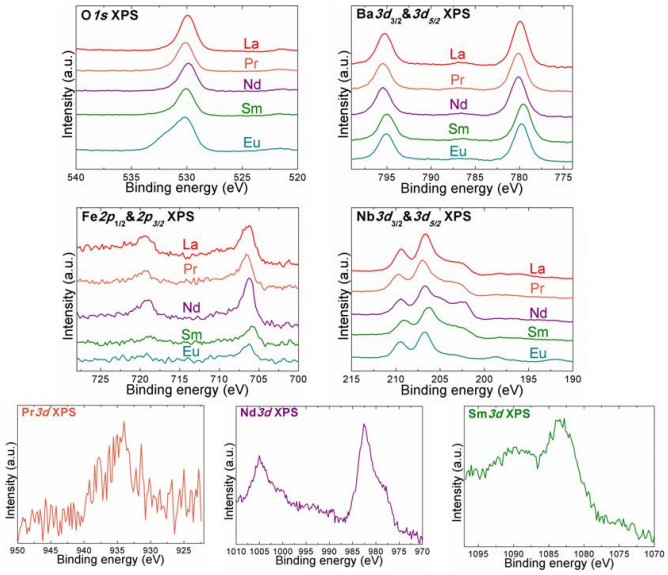

Figure 4. Line XPS spectra of O*1s*, Ba*3d*, Fe*2p*, Nb*3d* and Ln*3d* (except Eu) on BLnFNO crystals (Ln = Pr, Nd, Sm, Eu) after 120 sec. Ar etching.

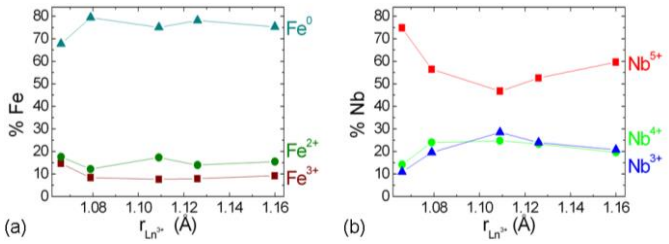

Figure 5. Component area (%) of (a) iron and (b) niobium extracted from fits of the XPS data obtained after 120 sec. Ar etching. (Solid lines are guides for the eyes).

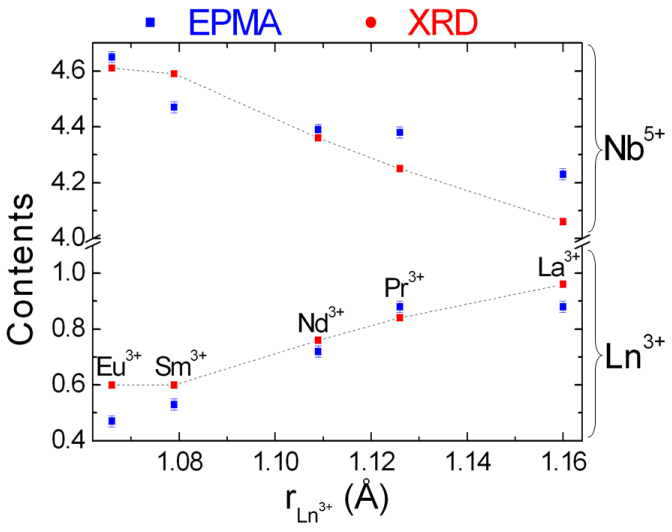

Figure 6. Evolution of niobium and lanthanides contents, as in BLnFNO crystals, extracted from EPMA analysis (blue) and XRD refinement (red). Dash lines correspond to the theoretical values associated with the formulation $Ba_2Ln_{1-x}\square_xFe_{1-3x/2}Nb_{4+3x/2}O_{15}$.

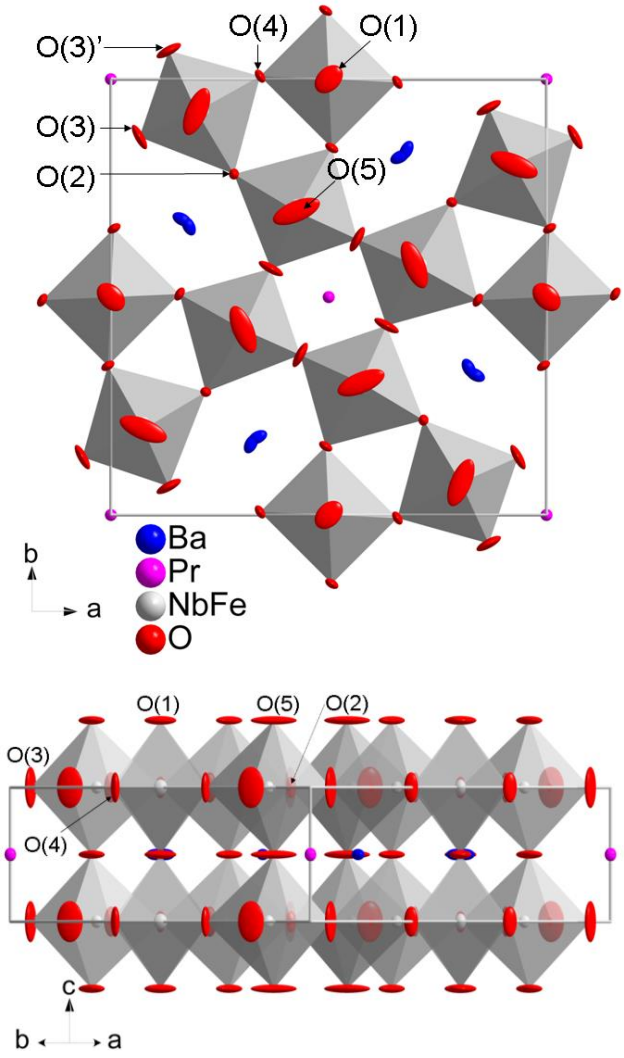

Figure 7. Crystal structure of BPrFNO at room temperature projected on the *ab* plane and along the [110] direction. The anisotropic displacement parameters of the atoms are indicated by 65% probability displacement ellipsoids.

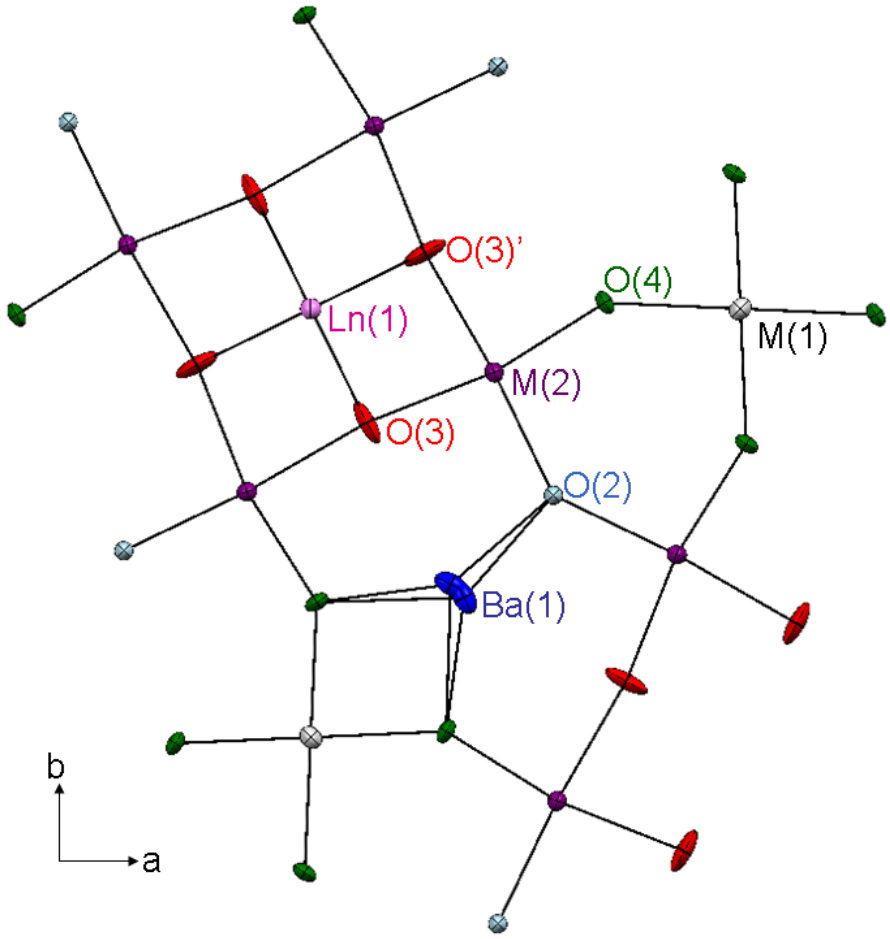

Figure 8. Identification of the atomic positions used for discussion of various crystal chemical parameters.

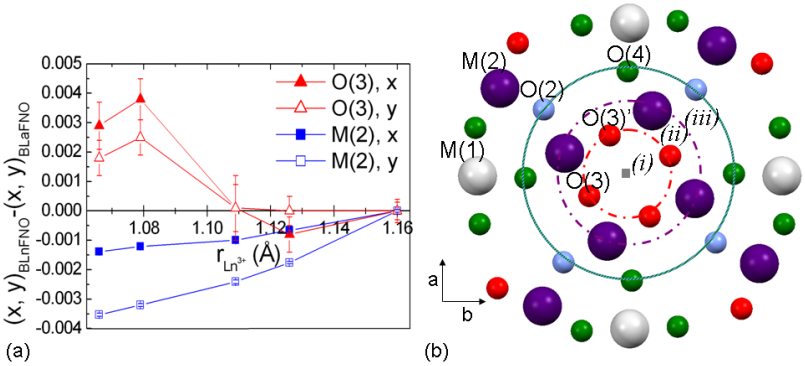

Figure 9. (a) Variation of atomic position in BLnFNO single-crystals with respect to BLaFNO positions, used as reference[18]. (Solid lines are guides for the eyes). (b) Section of the crystal structure in *ab* plane at z=0. Lanthanides accommodation in square site (Wyckoff position 0 0 ½) influences the atomic positions of (i) O(3), (ii) M(2), (iii) O(2) et O(4).

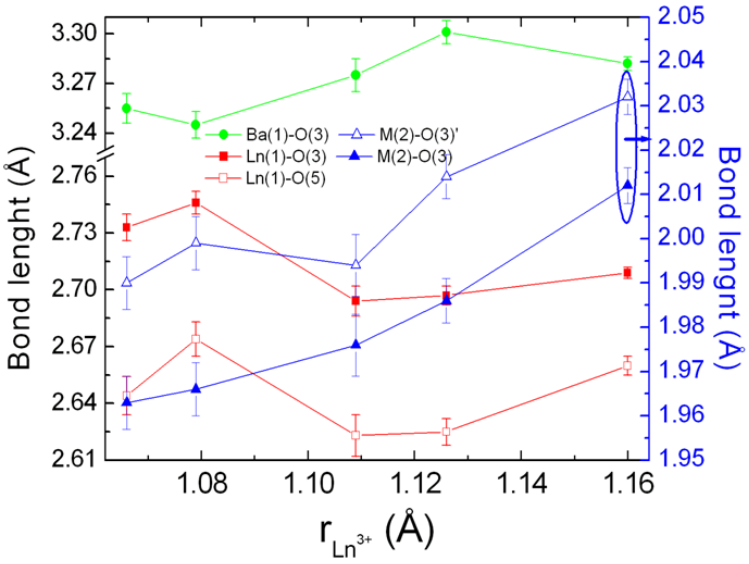

Figure 10. Evolution of selected Ba-O, Ln-O and M(2)-O bond length with respect to the ionic radii of Ln^{3+} ions.

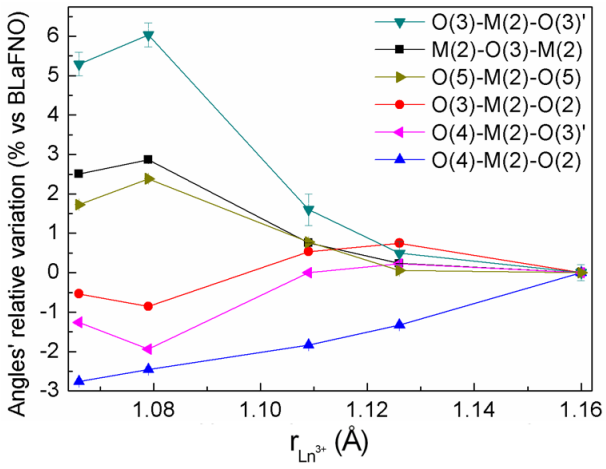

Figure 11. Relative variations (with reference to BLaFNO) of the various angles associated to the $[M(2)O_6]$ octahedra, plotted with respect to Ln^{3+} ionic radii.

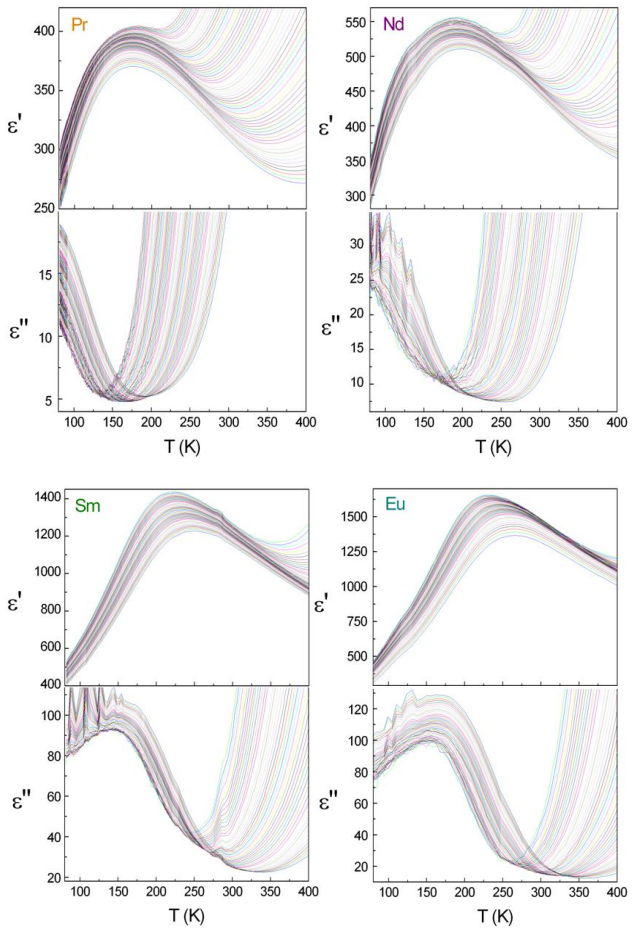

Figure 12. Real and imaginary part of the dielectric permittivity reported for BLnFNO crystals (f=[10kHz-1MHz]).

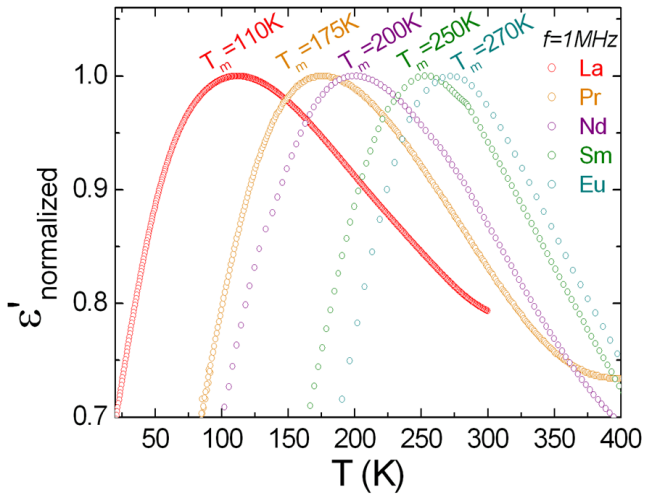

Figure 13. Thermal variation of the normalized dielectric permittivity at the frequency f=1MHz for BLnFNO crystals.

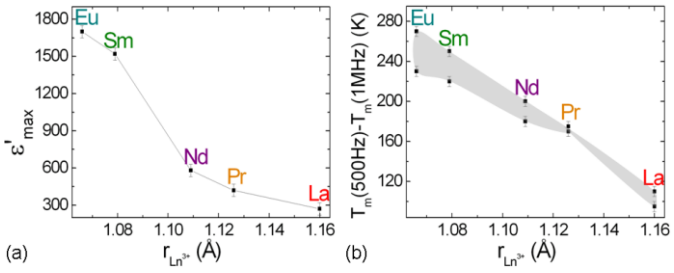

Figure 14. (a) Evolution of the maximum dielectric permittivity (at lowest frequency, 10kHz, solid lines are guides for the eyes). (b) Plot of T_m(500Hz) and T_m(1MHz), the grayed area highlighting the dielectric dispersion ΔT_m for the BLnFNO crystals (NB: dispersion in Pr sample is artificially reduced by dielectric losses).

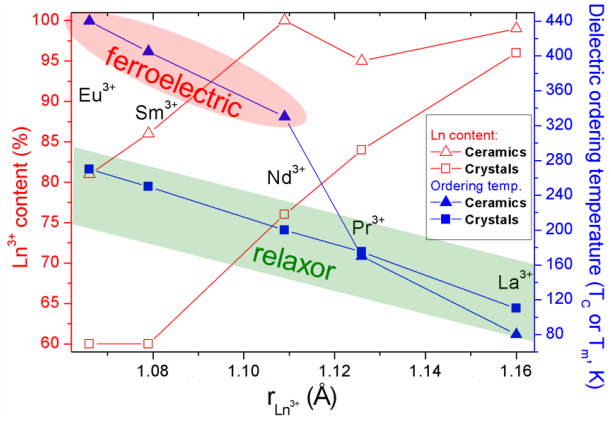

Figure 15. Evolution of dielectric ordering temperatures and Ln^{3+} contents (as determined from XRD) in single crystals and ceramics with respect to Ln^{3+} ionic radius. (Solid lines are guide for the eyes).

Table 1. Cationic contents, determined using EPMA, assuming a 100% filled octahedral framework.

Crystals	Ba *(th.: 2)*	Ln *(th.: 1)*	Fe *(th.: 1)*	Nb *(th.: 4)*	O
BLaFNO[18]	2.03(2)	0.88(2)	0.77(2)	4.23(2)	15.08(2)
BPrFNO	2.01(2)	0.88(2)	0.62(2)	4.38(2)	15.21(2)
BNdFNO	2.06(2)	0.72(2)	0.61(2)	4.39(2)	15.03(2)
BSmFNO	2.08(2)	0.53(2)	0.53(2)	4.47(2)	14.85(2)
BEuFNO	2.13(2)	0.47(2)	0.35(2)	4.65(2)	14.99(2)

Table 2. Gaussian-Lorentzian fitting results of Ba*3d*, Ln*3d*, Fe*2p* and Nb*3d* core levels after 120 sec. Ar etching time on BLnFNO crystals.

	Ba*3d*	Ln*3d*	Fe*2p*			Nb*3d*		
BLaFNO								
Cation	Ba^{2+}	Ln^{3+}	Fe^{3+}	Fe^{2+}	Fe^{0}	Nb^{5+}	Nb^{4+}	Nb^{3+}
BE (eV)	781.0(1)	835.3(1)	711.5(1)	709.6(1)	707.4(1)	207.6(1)	205.2(1)	203.5(1)
FWHM (eV)	2.1(1)	1.9(1)	1.8(1)	2.2(1)	2.0(1)	1.9(1)	2.0(1)	1.9(1)
Area (%)			9.2(1)	15.5(1)	75.3(1)	59.6(1)	19.7(1)	20.7(1)
BPrFNO								
BE (eV)	780.8(1)	934.8(1)	711.6(1)	709.1(1)	707.1(1)	207.5(1)	205.1(1)	203.5(1)
FWHM (eV)	2.1(1)	3.5(1)	1.7(1)	2.0(1)	1.7(1)	1.9(1)	1.9(1)	1.9(1)
Area (%)			7.9(1)	14.0(1)	78.1(1)	52.6(1)	23.4(1)	24.0(1)
BNdFNO								
BE (eV)	781.1(1)	983.4(1)	711.4(1)	709.1(1)	707.2(1)	207.8(1)	204.9(1)	203.3(1)
FWHM (eV)	2.2(1)	3.5(1)	1.5(1)	2.3(1)	1.5(1)	2.0(1)	2.0(1)	1.7(1)
Area (%)			7.6(1)	17.3(1)	75.1(1)	46.8(1)	24.7(1)	28.5(1)
BSmFNO								
BE (eV)	781.0(1)	1084.9(1)	711.3(1)	709.2(1)	707.2(1)	207.7(1)	205.2(1)	203.6(1)
FWHM (eV)	2.2 (1)	5.4(1)	1.5(1)	2.1(1)	1.3(1)	2.0(1)	2.1(1)	1.9(1)
Area (%)			8.4(1)	12.2(1)	79.4(1)	56.4(1)	24.0(1)	19.6(1)
BEuFNO								
BE (eV)	780.8(1)		711.4(1)	709.7(1)	707.4(1)	207.7(1)	205.6(1)	204.0(1)
FWHM (eV)	2.1(1)		1.8(1)	2.0(1)	2.0(1)	1.8(1)	2.0(1)	1.9(1)
Area (%)			14.7(1)	17.6(1)	67.7(1)	74.9(1)	14.2(1)	10.9(1)

Table 3. Gaussian-Lorentzian fitting results of O*1s* core levels after 120 sec. Ar etching time on BLnFNO crystals.

	(Fe,Nb)-O	Ln-O	Ba-O
BLaFNO			
BE (eV)	533.0(1)	531.7(1)	530.9(1)
FWHM (eV)	1.7(1)	1.7(1)	1.7(1)
Area (%)	5.8(1)	10.3(1)	83.9(1)
BPrFNO			
BE (eV)	532.8(1)	531.5(1)	530.7(1)
FWHM (eV)	1.9(1)	1.9(1)	1.7(1)
Area (%)	5.9(1)	12.8(1)	81.3(1)
BNdFNO			
BE (eV)	532.9(1)	531.6(1)	530.8(1)
FWHM (eV)	2.0(1)	1.5(1)	1.6(1)
Area (%)	7.0(1)	17.4(1)	75.6(1)
BSmFNO			
BE (eV)	533.5(1)	532.4(1)	531.4(1)
FWHM (eV)	2.0(1)	1.5(1)	1.6(1)
Area (%)	8.8(1)	13.8(1)	77.5(1)
BEuFNO			
BE (eV)	533.6(1)	532.9(1)	531.0(1)
FWHM (eV)	2.0(1)	2.0(1)	1.9(1)
Area (%)	13.7(1)	28.3(1)	58.0(1)

Table 4. Crystallographic data and agreement factors for BLnFNO single crystals, in the space group P4/mbm at room temperature.

	Crystallographic data			Agreement factors		
	a (Å)	c (Å)	V (Å^3)	R	wR	S
BLaFNO[18]	12.5202(2)	3.9364(1)	617.05(2)	0.0272	0.0534	1.176
BPrFNO	12.4899(2)	3.9266(1)	612.54(2)	0.0274	0.0586	1.159
BNdFNO	12.4408(2)	3.9144(1)	605.85(2)	0.0416	0.1021	1.323
BSmFNO	12.4911(2)	3.9391(1)	614.61(2)	0.0328	0.0849	1.273
BEuFNO	12.4707(2)	3.9345(1)	611.89(2)	0.0357	0.0933	1.163

Table 5. Occupancy (%) and crystal's chemical compositions determined by single crystals XRD analyses.

	Ba	Ln	Fe(1) / Fe(2)	Nb(1) / Nb(2)
BLaFNO[18]	100	96 (1)	22 (1) / 18 (1)	78 (1) / 82 (1)
	$Ba_2La_{0.96(1)}\square_{0.04(1)}Fe_{0.94(1)}Nb_{4.06(1)}O_{15}$			
BPrFNO	100	84 (1)	15 (1) / 15 (1)	85 (1) / 85 (1)
	$Ba_2Pr_{0.84(1)}\square_{0.16(1)}Fe_{0.75(1)}Nb_{4.25(1)}O_{15}$			
BNdFNO	100	76 (1)	12 (1) / 13 (1)	88 (1) / 87 (1)
	$Ba_2Nd_{0.76(1)}\square_{0.24(1)}Fe_{0.64(1)}Nb_{4.36(1)}O_{15}$			
BSmFNO	100	60 (1)	9 (1) / 8 (1)	91 (1) / 92 (1)
	$Ba_2Sm_{0.60(1)}\square_{0.40(1)}Fe_{0.41(1)}Nb_{4.59(1)}O_{15}$			
BEuFNO	100	60 (1)	7 (1) / 8 (1)	93 (1) / 92 (1)
	$Ba_2Eu_{0.60(1)}\square_{0.40(1)}Fe_{0.39(1)}Nb_{4.61(1)}O_{15}$			

Table 6. Fractional atomic coordinates refined on BLnFNO from single crystal XRD. Atomic positions omitted in the table: Ln *2b* (0 0 1/2), M(1) *2d* (1/2 0 0) and O(1) at 2c (1/2 0 1/2).

		Ba *8j* (x, y, 1/2)	M(2) *8i* (x, y, 0)	O(2) *4g* (x, $\bar{x}$ +½, 0)	O(3) *8i* (x, y, 0)	O(4) *8i* (x, y, 0)	O(5) *8j* (x, y, 1/2)
BLaFNO[18]	x	0.3392(1)	0.07482(4)	0.2185(3)	0.1335(4)	0.3430(3)	0.0763(6)
	y	0.1797(1)	0.21511(4)		0.0655(3)	0.0070(3)	0.1983(5)
BPrFNO	x	0.3371(2)	0.07416(4)	0.2176(3)	0.1327(5)	0.3424(3)	0.0742(8)
	y	0.1785(3)	0.21335(4)		0.0655(4)	0.0070(3)	0.1966(6)
BNdFNO	x	0.3372(2)	0.07383(5)	0.2174(4)	0.1336(9)	0.3423(5)	0.0736(13)
	y	0.1790(3)	0.21270(5)		0.0656(7)	0.0070(5)	0.1976(10)
BSmFNO	x	0.3368(2)	0.07361(5)	0.2168(4)	0.1373(7)	0.3422(4)	0.0749(10)
	y	0.1795(2)	0.21191(5)		0.0680(6)	0.0074(4)	0.2005(9)
BEuFNO	x	0.3366(3)	0.07343(5)	0.2170(4)	0.1364(8)	0.3422(4)	0.0743(12)
	y	0.1792(3)	0.21158(5)		0.0673(6)	0.0070(5)	0.1986(9)